

K-Radar: 4D Radar Object Detection for Autonomous Driving in Various Weather Conditions

Dong-Hee Paek^{1*} Seung-Hyun Kong^{1†} Kevin Tirta Wijaya²

¹CCS Graduate School of Mobility

²Robotics Program

KAIST

{donghee.paek, skong, kevin.tirta}@kaist.ac.kr

Abstract

Unlike RGB cameras that use visible light bands (384~769 THz) and Lidars that use infrared bands (361~331 THz), Radars use relatively longer wavelength radio bands (77~81 GHz), resulting in robust measurements in adverse weathers. Unfortunately, existing Radar datasets only contain a relatively small number of samples compared to the existing camera and Lidar datasets. This may hinder the development of sophisticated data-driven deep learning techniques for Radar-based perception. Moreover, most of the existing Radar datasets only provide 3D Radar tensor (3DRT) data that contain power measurements along the Doppler, range, and azimuth dimensions. As there is no elevation information, it is challenging to estimate the 3D bounding box of an object from 3DRT. In this work, we introduce KAIST-Radar (K-Radar), a novel large-scale object detection dataset and benchmark that contains 35K frames of 4D Radar tensor (4DRT) data with power measurements along the Doppler, range, azimuth, and elevation dimensions, together with carefully annotated 3D bounding box labels of objects on the roads. K-Radar includes challenging driving conditions such as adverse weathers (fog, rain, and snow) on various road structures (urban, suburban roads, alleyways, and highways). In addition to the 4DRT, we provide auxiliary measurements from carefully calibrated high-resolution Lidars, surround stereo cameras, and RTK-GPS. We also provide 4DRT-based object detection baseline neural networks (baseline NNs) and show that the height information is crucial for 3D object detection. And by comparing the baseline NN with a similarly-structured Lidar-based neural network, we demonstrate that 4D Radar is a more robust sensor for adverse weather conditions. All codes are available at <https://github.com/kaist-avelab/k-radar>.

1 Introduction

An autonomous driving system generally consists of sequential modules of perception, planning, and control. As the planning and control modules rely on the output of the perception module, it is crucial for the perception module to be robust even under adverse driving conditions.

Recently, various works have proposed deep learning-based autonomous driving perception modules that demonstrate remarkable performances in lane detection (Paek et al., 2022; Liu et al., 2021), object detection (Wang et al., 2021a; Lang et al., 2019; Major et al., 2019), and other tasks (Ranftl et al., 2021; Teed and Deng, 2021). These works often use RGB images as the inputs to the neural networks due to the availability of numerous public large-scale datasets for camera-based perception. Moreover, an RGB image has a relatively simple data structure, where the data dimensionality is

*co-first authors

†corresponding author

relatively low and neighboring pixels often have high correlation. Such a simplicity enables deep neural networks to learn the underlying representations of images and recognize objects on the image.

Unfortunately, camera is prone to poor illumination, can easily be obscured by raindrops and snowflakes, and cannot preserve depth information that is crucial for accurate 3D scene understanding of the environment. On the other hand, Lidar actively emits measuring signals in the infrared spectrum, therefore, the measurements are hardly affected by illumination conditions. Lidar can also provide accurate depth measurements within centimeters resolution. However, Lidar measurements are still affected by adverse weathers since the wavelength of the signals ($\lambda=850\text{nm}\sim 1550\text{nm}$) is not long enough to pass through raindrops or snowflakes (Kurup and Bos, 2021).

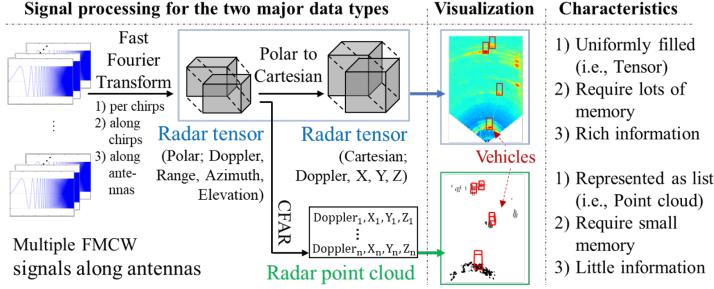


Figure 1: An overview of the signal processing of the FMCW Radar and a visualization of the two main data types (i.e., Radar tensor (RT) and Radar point cloud (RPC)). The RT is a dense data matrix with power measurements in all element along the dimensions through a Fast Fourier Transform (FFT) operation applied to FMCW signals. Since all elements are non-zero values, the RT provides dense information regarding the environment with minimal loss, at a cost of high memory requirement. On the other hand, the RPC is a data type in which target (i.e., object candidate group) information is extracted in the form of a point cloud with a small amount of memory by applying Constant False Alarm Rate (CFAR) algorithm to the RT. Due to the ease of implementing FFT and CFAR directly on the hardware, many Radar sensors provide RPCs as output. However, the RPC may lose a significant amount of information regarding the environment due to the CFAR algorithm.

Similar to Lidar, a Radar sensor actively emits waves and measures the reflection. However, Radar emits radio waves ($\lambda \approx 4\text{mm}$) that can pass through raindrops and snowflakes. As a result, Radar measurements are robust to both poor illumination and adverse weather conditions. This robustness is demonstrated in (Abdu et al., 2021), where a Frequency Modulated Continuous Wave (FMCW) Radar-based perception module is shown to be accurate even in adverse weather conditions and can be easily implemented directly on the hardware.

As FMCW Radars with dense Radar tensor (RT) outputs become readily available, numerous works (Dong et al., 2020; Mostajabi et al., 2020; Sheeny et al., 2021) propose RT-based object detection networks with comparable detection performance to camera

and Lidar-based object detection networks. However, these works are limited to 2D bird-eye-view (BEV) object detection, since FMCW Radars utilized in existing works only provide 3D Radar tensor (3DRT) with power measurements along the Doppler, range, and azimuth dimensions.

In this work, we introduce KAIST-Radar (K-Radar), a novel 4D Radar tensor (4DRT)-based 3D object detection dataset and benchmark. Unlike the conventional 3DRT, 4DRT contains power measurements along the Doppler, range, azimuth, and elevation dimensions so that the 3D spatial information can be preserved, which could enable accurate 3D perception such as 3D object detection with Lidar. To the best of our knowledge, K-Radar is the first large-scale 4DRT-based dataset and benchmark, with 35k frames collected from various road structures (e.g. urban, suburban, highways), time (e.g. day, night), and weather conditions (e.g. clear, fog, rain, snow). In addition to the 4DRT, K-Radar also provides high-resolution Lidar point clouds (LPCs), surround RGB images from four stereo cameras, and RTK-GPS and IMU data of the ego-vehicle.

Since the 4DRT high-dimensional representation is unintuitive to human, we leverage the high-resolution LPC so that the annotators can accurately label the 3D bounding boxes of objects on the road in the visualized point clouds. The 3D bounding boxes can be easily transformed from the Lidar to the Radar coordinate frame since we provide both spatial and temporal calibration parameters to correct offsets due to the separations of the sensors and the asynchronous measurements, respectively. K-Radar also provides a unique tracking ID for each annotated object that is useful for tracking

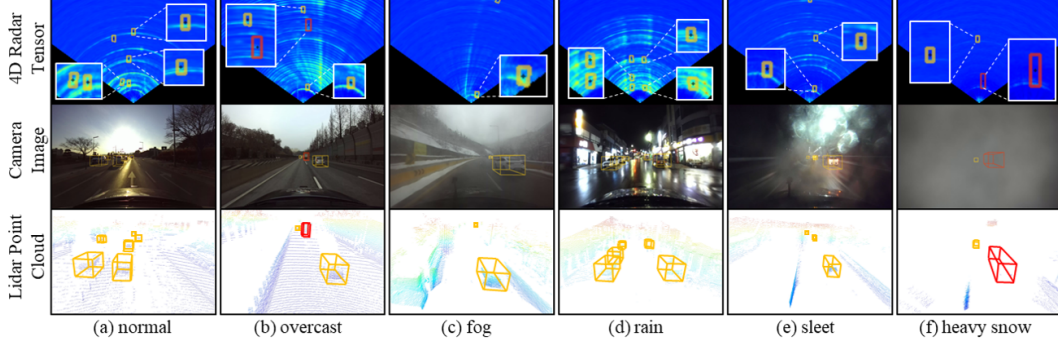


Figure 2: Samples of K-Radar datasets for various weather conditions. Each column shows (1) 4DRTs, (2) front view camera images, and (3) Lidar point clouds (LPCs) of different weather conditions. 4DRTs are represented in a two-dimensional (BEV) Cartesian coordinate system using a series of visualization processes that are described in Section 3.3. In this example, yellow and red bounding boxes represent the sedan and bus or truck classes, respectively. Appendix A contains further samples of K-Radar datasets for each weather condition.

an object along a sequence of frames. Examples of information regarding tracking are shown in Appendix I.7.

To demonstrate the necessity of 4DRT-based perception module, we present a 3D object detection baseline neural network (baseline NN) that directly consumes 4DRT as an input. From the experimental results on K-Radar, we observe that the 4DRT-based baseline NN outperforms the Lidar-based network in the 3D object detection task, especially in adverse weather conditions. We also show that the 4DRT-based baseline NN utilizing height information significantly outperforms network that only utilizes BEV information. Additionally, we publish the complete development kits (devkits) that include: (1) training / evaluation codes for 4DRT-based neural networks, (2) labeling / calibration tools, and (3) visualization tools to accelerate research in the field of 4DRT-based perception.

In a summary, our contributions are as follow,

- We present a novel 4DRT-based dataset and benchmark, K-Radar, for 3D object detection. To the best of our knowledge, K-Radar is the first large-scale 4DRT-based dataset and benchmark with diverse and challenging illumination, time, and weather conditions. With the carefully annotated 3D bounding box labels and multimodal sensors, K-Radar can also be used for other autonomous driving tasks such as object tracking and odometry.
- We propose a 3D object detection baseline NN that directly consumes 4DRT as an input and verify that the height information of 4DRT is essential for 3D object detection. We also demonstrate the robustness of 4DRT-based perception for autonomous driving, especially under adverse weather conditions.
- We provide devkits that include: (1) training/evaluation, (2) labeling/calibration, and (3) visualization tools to accelerate 4DRT-based perception for autonomous driving research.

The remaining of this paper is organized as follows. Section 2 introduces existing datasets and benchmarks that are related to perception for autonomous driving. Section 3 explains the K-Radar dataset and baseline NNs. Section 4 discusses the experimental results of the baseline NN on the K-Radar dataset. Section 5 concludes the paper with a summary and discussion on the limitations of this study.

2 Related Works

Deep neural networks generally require a large amount of training samples collected from diverse conditions so that they can achieve remarkable performance with excellent generalization. In autonomous driving, there are numerous object detection datasets that provide large-scale data of various sensor modalities, shown in Table 1.

Table 1: Comparison of object detection datasets and benchmarks for autonomous driving. HR and LR refer to High Resolution Lidar with more than 64 channels and Low Resolution with less than 32 channels, respectively. Bbox., Tr.ID, and Odom. refer to bounding box annotation, tracking ID, and odometry, respectively. Bold text indicates the best entry in each category.

Data -set	Num. data	Sensors					Label		
		RT	RPC	LPC	Camera	GPS	Bbox.	Tr. ID	Odom.
K-Radar (ours)	35K	4D	4D	HR.	360.	RTK	3D	O	O
VoD	8.7K	X	4D	HR.	Front	RTK	3D	O	O
Astyx	0.5K	X	4D	LR.	Front	X	3D	X	X
RADDet	10K	3D	3D	X	Front	X	2D	X	X
Zendar	4.8K	3D	3D	LR.	Front	GPS	2D	O	O
RADIATE	44K	3D	3D	LR.	Front	GPS	2D	O	O
CARRADA	12.6K	3D	3D	X	Front	X	2D	O	X
CRUW	396K	3D	3D	X	Front	X	Point	O	X
NuScenes	40K	X	3D	LR.	360.	RTK	3D	O	O
Waymo	230K	X	X	HR.	360.	X	3D	O	X
KITTI	15K	X	X	HR.	Front	RTK	3D	O	O
BDD100k	120M	X	X	X	Front	RTK	2D	O	O

KITTI (Geiger et al., 2012) is one of the earliest and widely-used datasets for autonomous driving object detection that provide camera and Lidar measurements along with accurate calibration parameters and 3D bounding box labels. However, the number of samples and the diversity of the dataset is relatively limited since the 15K frames of the dataset are collected mostly in urban areas during daytime. Waymo (Sun et al., 2020) and NuScenes (Caesar et al., 2020) on the other hand provide a significantly larger number of samples with 230K and 40K frames, respectively. In both datasets, the frames are collected during both daytime and nighttime, increasing the diversity of the datasets. Additionally, NuScenes provides 3D Radar point clouds (RPC), and Nabati and Qi (2021) demonstrates that utilizing Radar as an auxiliary input to the neural network can improve the detection performance of the network. However, RPC lose a substantial amount of information due to the CFAR thresholding operation and result in inferior detection performance when being used as the primary input to the network. For example, the state-of-the-art performance of Lidar-based 3D object detection on NuScenes dataset is 69.7% mAP, whereas for Radar-based is only 4.9% mAP.

In the literature, there are several 3DRT-based object detection datasets for autonomous driving. CARRADA (Ouaknine et al., 2021) provides Radar tensors in the range-azimuth and range-Doppler dimensions with labels of up to two objects in a controlled environment (wide flat surface). Zendar (Mostajabi et al., 2020), RADIATE (Sheeny et al., 2021), and RADDet (Zhang et al., 2021) on the other hand provide Radar tensors collected on real road environments, but can only provide 2D BEV bounding box labels due to the lack of height information in 3DRTs. CRUW (Wang et al., 2021b) provides a large number of 3DRTs, but annotations only provide 2D point locations of objects. VoD (Palffy et al., 2022) and Asyx (Meyer and Kusch, 2019) provide 3D bounding box labels with 4DRPCs. However, the dense 4DRTs are not made available, and the number of samples in the datasets is relatively small (i.e., 8.7K and 0.5K frames). To the best of our knowledge, the proposed K-Radar is the first large-scale dataset that provide 4DRT measurements on diverse conditions along with 3D bounding box labels.

Table 2: Comparison of object detection datasets and benchmarks for autonomous driving. d/n refers to day and night. Bold text indicates the best entry in each category.

Dataset	Weather conditions	Time
K-Radar (ours)	overcast, fog, rain, sleet, snow	d/n
VoD	X	day
Astyx	X	day
RADDet	X	day
Zendar	X	day
RADIATE	overcast, fog, rain, snow	d/n
CARRADA	X	day
CRUW	X	day
NuScenes	overcast, rain	d/n
Waymo	overcast	d/n
KITTI	X	day
BDD100k	overcast, fog, rain, snow	d/n

5

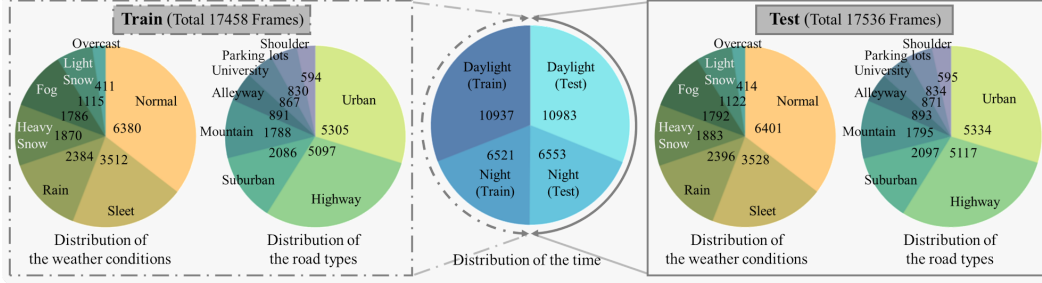


Figure 4: Distribution of data over collection time (night/day), weather conditions, and road types. The central pie chart shows the distribution of data over collection time, while the left and right pie charts show the distribution of data over weather conditions and road types for the train and test sets, respectively. At the outer edges of each pie chart, we state the collection time, weather conditions, and road types, and at the inner part, we state the number of frames in each distribution.

urban environments are mostly collected in Daejeon of the Republic of Korea. The data collection process results in 35K frames of multi-modal sensor measurements that constitute the K-Radar dataset. We classify the collected data into several categories according to the criteria listed on Appendix C. In addition, we split the dataset into training and test sets in a way that each condition appears in both sets in a balanced manner, as shown in Figure 4.

In total, there are 93.3K 3D bounding box labels for objects (i.e., sedan, bus or truck, pedestrian, bicycle, and motorcycle) on the road within the longitudinal radius of 120m and lateral radius of 80m from the ego-vehicle. Note that we only annotate objects that appear in the positive longitudinal axis, i.e., in front of the ego-vehicle.

In Figure 5, we show the distribution of object classes and object distances from the ego-vehicle in the K-Radar dataset. The majority of objects lie within 60m distance from the ego-vehicle, with 10K~15K objects appearing in each of the 0m~20m, 20m~40m, and 40m~60m distance categories, and around 7K objects appearing in over 60m distance category. As a result, K-Radar can be used to evaluate the performance of a 3D object detection networks for objects on various distances.

3.3 Data visualization, calibration, and annotation processes

Contrary to the 3D Radar tensor (3DRT) that lacks height information, 4D Radar tensor (4DRT) is a dense data tensor filled with power measurements in four dimensions: Doppler, range, azimuth, and elevation. However, the additional dimensionality of dense data imposes a challenge in visualizing 4DRT as a sparse data such as a point cloud (Figure 2). To cope with the problem, we visualize 4DRT as a two-dimensional heat map in the Cartesian coordinate system through heuristic processing as shown in Figure 6-(a), which results in 2D heatmap visualizations in the bird-eye-view (BEV-2D), front-view (FV-2D), and side-view (SV-2D). We refer to these 2D heatmaps collectively as BFS-2D.

Through the BEV-2D, we can intuitively verify the robustness of 4D Radars to adverse weather conditions as shown in Figure 2. As mentioned earlier, camera and Lidar measurements can deteriorate under adverse weather conditions such as rain, sleet, and snow. In Figure 2-(e,f), we show that the measurements of a Lidar for a long-distance object are lost in heavy snow conditions. However, the

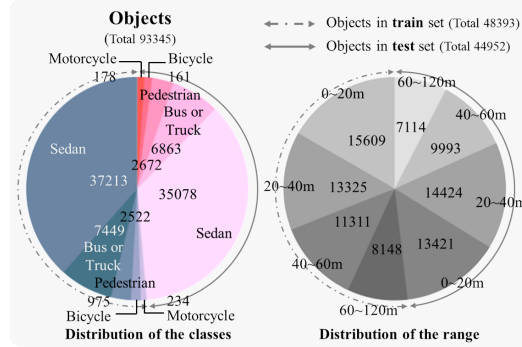


Figure 5: Objects classes and distance-to-ego-vehicle distribution for the training/test splits provided in the K-Radar dataset. We state the object class name and distance to the ego-vehicle in the outer part of the piechart, and the number of objects in each distribution in the inner part of the pie chart.

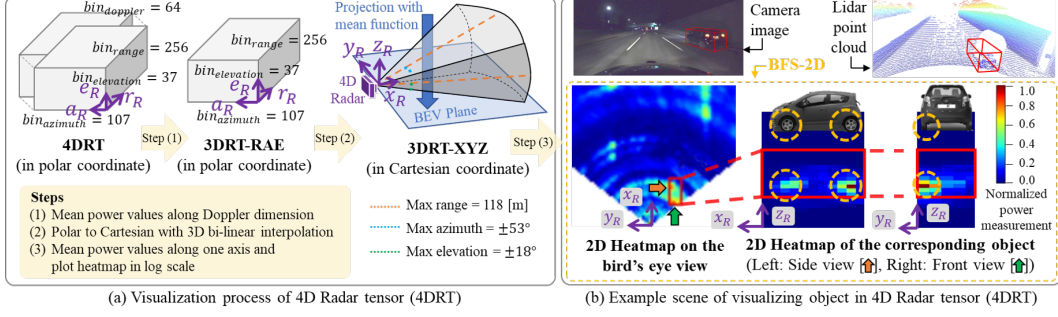


Figure 6: (a) A 4DRT visualization process and (b) the 4DRT visualization results. (a) is the process of visualizing 4DRT (polar coordinate) into BFS-2D (Cartesian coordinate) through a three-step process: (1) extracting the 3D Radar tensor that contains measurements along the range, azimuth, and elevation dimensions (3DRT-RAE) by reducing the Doppler dimension of the 4DRT through dimension-wise averaging, (2) transforming the 3DRT-RAE (polar coordinate) into 3DRT-XYZ (Cartesian coordinate), (3) by removing one of the three dimensions of 3DRT-XYZ, the 4DRT is finally visualized as a two-dimensional Cartesian coordinate system. (b) is an example in which 4DRT-3D information is visualized as BFS-2D through the process of (a). We also show the front view camera image and the LPC of the same frame on the upper side of (b), and the bounding box of the car is marked in red. As shown in (b), the 4DRT is represented by three types of views (i.e., BEV, side view, and front view). We note that high power measurements are observed on wheels rather than the body of the vehicle when compared to the actual vehicle model picture with the side view and front view of the object. This is because radio wave reflection occurs mainly in wheels made of metal (Briskin et al., 2018), not in the body of a vehicle made of reinforced plastic.

BEV-2D of the 4DRT clearly indicate the object with high-power measurements on the edge of the bounding box of the objects.

Even with the BFS-2D, it is still challenging for a human annotator to recognize the shape of objects appearing on the frame and accurately annotate the corresponding 3D bounding boxes. Therefore, we create a tool that enables 3D bounding boxes annotation in LPCs where object shapes are more recognizable. In addition, we use the BEV-2D to help the annotators in the case of lost Lidar measurements due to adverse weather conditions. The details are covered in Appendix D.1.

We also present a tool for frame-by-frame calibration of the BEV-2D and the LPC to transform the 3D bounding box labels from the Lidar coordinate frame to the 4D Radar coordinate frame. The calibration tool supports a resolution of 1 cm per pixel with a maximum error of 0.5 cm. The details of calibration between 4D Radar and Lidar are covered in Appendix D.2.

Additionally, we precisely obtain the calibration parameter between Lidar and the camera through a series of processes detailed in Appendix D.3. The calibration process between Lidar and camera enables the 3D bounding boxes and LPCs to be projected accurately onto camera images, which is crucial for multi-modal sensor fusion study, and can be used to produce dense depth maps for monocular depth estimation study.

3.4 Baseline NNs for K-Radar

We provide two baseline NNs to demonstrate the importance of height information for 3D object detection: (1) Radar Tensor Network with Height (RTNH) that extracts feature maps (FMs) from RT with 3D Sparse CNN so that height information is utilized, and (2) Radar Tensor Network without Height (RTN) that extracts FMs from RT with 2D CNN that does not utilize height information.

As shown in Figure 7, both RTNH and RTN consist of pre-processing, backbone, neck, and head. The pre-processing transforms the 4DRT from polar to Cartesian coordinate frame and extracts a 3DRT-XYZ within the region of interest (RoI). Note that we reduce the Doppler dimension by taking the mean value along the dimension. The backbone then extracts FMs that contain important features for the bounding box predictions. And the head predicts 3D bounding boxes from the concatenated FM produced by the neck.

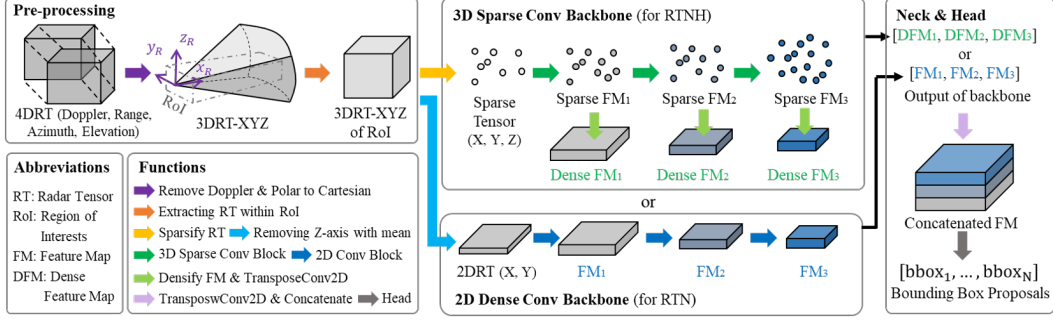


Figure 7: Two baseline NNs for verifying 4DRT-based 3D object detection performance.

The network structure of RTNH and RTN, described in details in Appendix E, is similar except the backbone. We construct the backbones of RTNH and RTN with 3D Sparse Conv Backbone (3D-SCB) and 2D Dense Conv Backbone (2D-DCB), respectively. 3D-SCB utilizes 3D sparse convolution (Liu et al., 2015) so that the three-dimensional spatial information (X, Y, Z) can be encoded into the final FM. We opt to use the sparse convolution on sparse RT (top-10% power measurements in the RT) since dense convolution on the original RT requires a prohibitively large amount of memory and computations that are unsuitable for real-time autonomous driving applications. Unlike 3D-SCB, 2D-DCB uses 2D convolution so that only two-dimensional spatial information (X, Y) is encoded into the final FM. As a result, the final FM produced by 3D-SCB contains 3D information (with height), whilst the final FM produced by 2D-DCB only contains 2D information (without height).

4 Experiment

In this section, we demonstrate the robustness of 4DRT-based perception for autonomous driving under various weathers in order to find 3D object detection performance comparison between the baseline NN and a similarly-structured Lidar-based NN, PointPillars (Lang et al., 2019). We also discuss the importance of height information by comparing 3D object detection performance between baseline NN with 3D-SCB backbone (RTNH) and baseline NN with 2D-DCB backbone (RTN).

4.1 Experiment Setup and Metric

Implementation Detail We implement the baseline NNs and PointPillars using PyTorch 1.11.0 on Ubuntu machines with a RTX3090 GPU. We set the batch size to 4 and train the networks for 11 epochs using Adam optimizer with a learning rate of 0.001. Note that we set the detection target to the sedan class, which has the largest number of samples in K-Radar dataset.

Metric In the experiments, we utilize the widely-used Intersection Over Union (IOU)-based Average Precision (AP) metric to evaluate the 3D object detection performance. We provide APs for BEV (AP_{BEV}) and 3D (AP_{3D}) bounding boxes predictions as in (Geiger et al., 2012), where a prediction is considered to be a true positive if the IoU is over 0.3.

Table 3: Performance comparison of baseline NNs with or without height Information.

Baseline NNs	AP_{3D} [%]	AP_{BEV} [%]	GPU RAM [MB]
RTNH	47.44	58.39	421
RTN	40.12	50.67	520

4.2 Comparison between RTN and RTNH

We show the detection performance comparison between RTNH and RTN on Table 3. We can observe that RTNH has 7.32% and 7.72% higher performance in AP_{3D} and AP_{BEV} , respectively, compared to RTN. RTNH significantly surpasses RTN in terms of both AP_{3D} and AP_{BEV} , indicating the importance of height information available in the 4DRT for 3D object detection. Furthermore, RTNH requires less GPU memory compared to RTN since it utilizes the memory-efficient sparse convolutions as mentioned in Section 3.4.

4.3 Comparison between RTNH and PointPillars

Table 4: Performance comparison of NNs of Radar and Lidar under various weather conditions

Networks	Metric	Total	normal	over-cast	fog	rain	sleet	light snow	heavy snow
RTNH (4D Radar)	$AP_{3D}[\%]$	47.4	49.9	56.7	52.8	42.0	41.5	50.6	44.5
	$AP_{BEV}[\%]$	58.4	58.5	64.2	76.2	58.4	60.3	57.6	56.6
PointPillars (Lidar)	$AP_{3D}[\%]$	45.4	52.3	56.0	42.2	44.5	22.7	40.6	29.7
	$AP_{BEV}[\%]$	49.3	56.6	61.0	52.0	57.8	23.1	51.6	30.8

We show the detection performance comparison between RTNH and a similarly-structured Lidar-based detection network, PointPillars, in Table 4. The Lidar-based network suffers significant BEV and 3D detection performance drops of 33.5% and 29.6% or 25.8% and 22.6%, respectively, in sleet or heavy snow condition compared to the normal condition. In contrast, the 4D radar-based RTNH detection performance is hardly affected by adverse weathers, where the BEV and 3D object detection performances in sleet or heavy snow condition are better or similar compared to the normal condition. The results testify the robustness of 4D radar-based perception in adverse weathers. We provide qualitative results and additional discussions for other weather conditions in Appendix F.

5 Limitation and Conclusion

In this section, we discuss the limitations of K-Radar and provide a summary of this work, along with suggestions on the future research directions.

5.1 Limitation of the FOV coverage of 4DRTs

As mentioned in Section 3.1, K-Radar provides 4D radar measurements in the forward direction, with an FOV of 107 degree. The measurement coverage is more limited compared to the 360 degree FOV of Lidar and camera. This limitation is originated from the size of a 4DRT with dense measurements in four dimensions, which require significantly larger memory to store the data compared to a camera image with two dimensions or a LPC with three dimensions. Specifically, the size of the 4DRT data in K-Radar is roughly 12TB, while the size of surround camera images data is about 0.4TB, and the size of LPCs data is about 0.6TB. Since providing 360 degrees 4DRT measurements requires a prohibitively large amount of memory, we opt to record 4DRT data only in the forward direction, which could provide the most relevant information for autonomous driving.

5.2 Conclusion

In this paper, we have introduced a 4DRT-based 3D object detection dataset and benchmark, K-Radar. The K-Radar dataset consists of 35K frames with 4DRT, LPC, surround camera images, and RTK-IMU data, all of which are collected in various time and weather conditions. K-Radar provides 3D bounding box labels and tracking ID for 93.3K objects of five classes with distance of up to 120 m. To verify the robustness of 4D radar-based object detection, we introduce baseline NNs that uses 4DRT as the input. From experimental results, we demonstrate the importance of height information that is not available in the conventional 3DRT and the robustness of 4D radar under adverse weathers. While the experiments in this work are focused on 4DRT-based 3D object detection, K-Radar can be used for 4DRT-based object tracking, SLAM, and various other perception tasks. Therefore, we hope that K-Radar can accelerate works in 4DRT-based perception for autonomous driving.

Acknowledgment

This work was partly supported by Institute of Information & communications Technology Planning & Evaluation (IITP) grant funded by the Korea government (MSIT) (No. 01210790) and the National Research Foundation of Korea (NRF) grant funded by the Korea government (MSIT) (No. 2021R1A2C3008370).

Appendix The appendix is organized as follows. We present details of the K-Radar dataset, the sensor suite, and criteria of conditions (weather conditions, road structures, and collection time) in Section A, B, and C, respectively. We also provide details of the annotation/calibration process and the baseline neural networks (NNs) in Section D and E, respectively. We discuss results regarding each weather condition and consideration of the K-Radar dataset as a pre-training dataset for other Radar tensor datasets in Section F and G, respectively. In addition, we report performance of RTNH on wider areas and multiple classes in Section H. Finally, we introduce details of devkits and list relevant URLs to help with understanding the content of the paper in Section I and J, respectively.

A Additional details for K-Radar dataset

In this section, we present additional samples of K-Radar dataset, sequence distribution, dataset composition, license, and privacy concerns.

A.1 Additional samples of the K-Radar dataset and explanation of LPCs for each weather condition

In the sleet (Figure 8-(e)) or heavy snow (Figure 8-(g)) condition, the Lidar point cloud (LPC) measurements of some objects ahead are lost when the ego-vehicle is driving. Conversely, in the rain (Figure 8-(d)) or light snow (Figure 8-(f)) condition, LPC measurements of objects exist. The reason

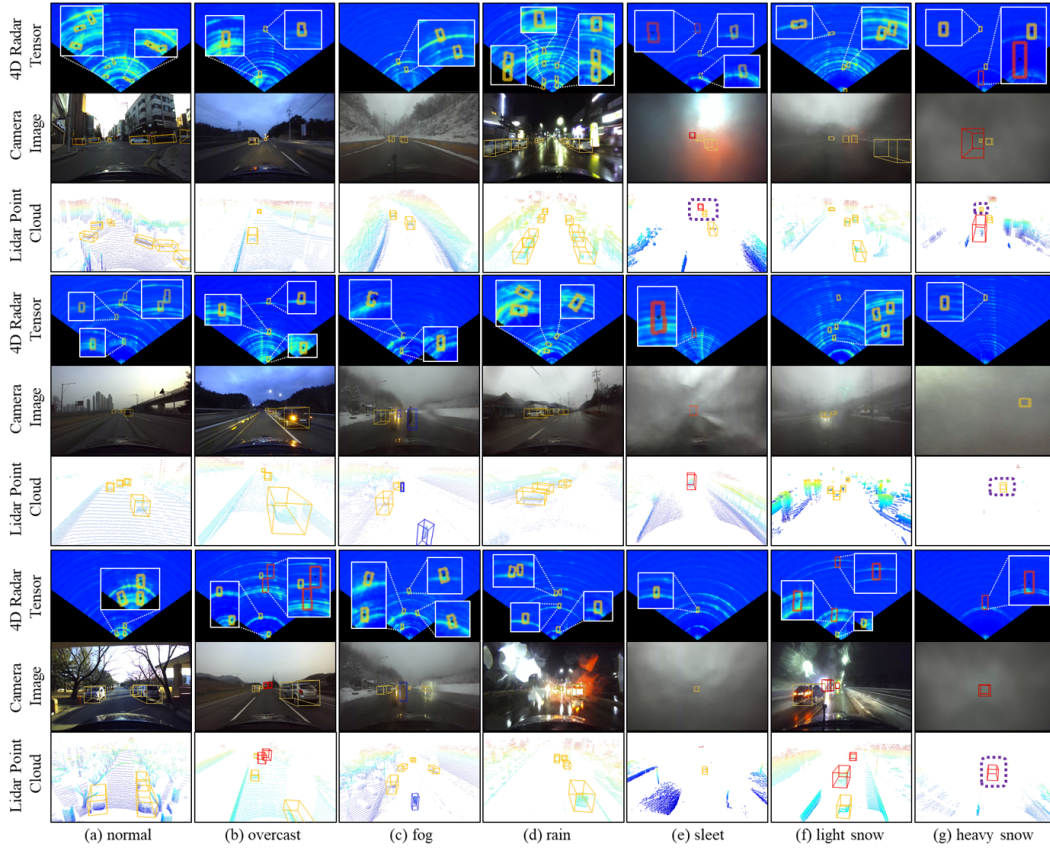


Figure 8: Additional samples of K-Radar datasets for various weather conditions. (1) 4DRTs, (2) front view camera images, and (3) Lidar point clouds (LPCs) of three different road conditions with the same weather condition are depicted in three boxes in each column. In this example, yellow, red, and blue bounding boxes represent the sedan, bus or truck, and pedestrian classes, respectively. Objects with all LPC measurements missing due to the adverse weather are marked with purple dotted lines. More samples of K-Radar dataset can be visualized using the devkits program described in Section I.

for this is as follows. Sleet is a mix of rain and snow that freezes when it falls from the sky in a liquid state and comes into contact with a sensor or an ego-vehicle colder than the air (Zhou et al., 2016). In our case, the sleet freezes on the front surface of the Lidar sensor, creating a layer of frost. Thus, as shown in Figure 8-(e), the measuring signals from the Lidar cannot reach objects in the front of the ego-vehicle, which results in missing points in the LPC. In addition, heavy snow is a weather condition in which snow falls over 1 cm per hour as described in Table 8, and Figure 3 shows that a lot of snow accumulates on the front surface of the sensor after the vehicle drives forward for 5 minutes. For this reason, similar to sleet, some LPC measurements of objects in front of the ego-vehicle are missing, as shown in Figure 8-(g). Unlike sleet and heavy snow, there is only a little-to-no amount of snow accumulation on the front surface of the Lidar sensor in light snow condition, as described in Table 8. In addition, LPC measurements of objects are also partially available in rain condition, since raindrops slip over the front surface of the Lidar sensor. Therefore, the Lidar sensors can measure objects in front of the ego-vehicle as shown in Figure 8-(d) and (f). Note that we provide a video clip (Figure 9) in Section J URL 2 to show sensor measurements collected while driving forward under the heavy snow condition.

A.2 Sequence distribution

The K-Radar dataset provides a total of 35K frame data obtained in different weather conditions, road structures, and collection time. The dataset is divided into 58 sequences, where the details of each sequence are shown in Table 5.

A.3 Dataset composition

Each of the 58 sequences consists of 12 compressed folders, as shown in Table 6. Table 6 provides information on the folder name, data type, extension, size, and the usage of each folder.

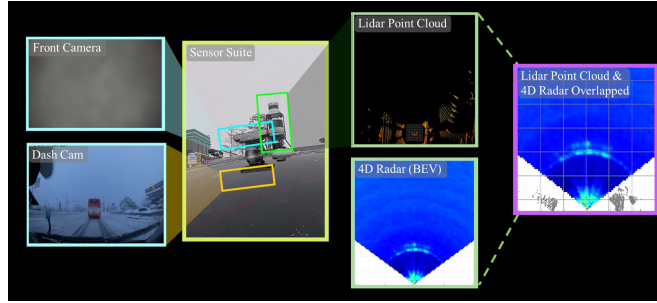


Figure 9: A snippet of the video clip that shows each sensor measurement dynamically changing during driving under the heavy snow condition. (see Section J URL 2)

A.4 License

The K-Radar dataset is published under the CC BY-NC-ND License, and all codes are published under the Apache License 2.0.

A.5 Privacy concerns

We confirm that all the image sequences with pedestrians, bicycles, and motorcycles do not have recognizable faces. Although everyone is wearing a mask due to COVID-19, we have taken additional precautions and blurred all faces to protect their privacy as shown in Figure 10.



Figure 10: Examples of front images showing people whose faces are blurred.

Table 5: Sequence of the K-Radar dataset; sequences 1 through 20 are obtained in Dae-jeon, and sequences 21 through 58 are obtained in Gang-won Province. ‘he. snow’ and ‘park.lot’ denotes heavy snow and parking lot, respectively.

Seq.	Num. Fr.	Weather Cond.	Road Stru.	Time	Seq.	Num. Fr.	Weather Cond.	Road Stru.	Time
1	597	normal	urban	night	30	470	sleet	park.lot	day
2	462	normal	highway	night	31	598	sleet	suburban	day
3	597	normal	highway	night	32	597	rain	suburban	day
4	588	normal	highway	night	33	598	rain	suburban	day
5	597	normal	urban	day	34	598	rain	suburban	night
6	594	normal	urban	night	35	597	sleet	park.lot	night
7	595	normal	alleyway	night	36	597	sleet	park.lot	night
8	567	normal	university	night	37	597	sleet	suburban	night
9	833	normal	highway	day	38	597	fog	mountain	day
10	1130	normal	highway	day	39	597	fog	mountain	day
11	1195	normal	highway	day	40	598	fog	mountain	day
12	888	normal	highway	day	41	597	fog	mountain	day
13	227	overcast	highway	day	42	598	light snow	urban	day
14	595	normal	urban	day	43	598	light snow	urban	day
15	591	normal	urban	day	44	597	fog	shoulder	day
16	578	normal	university	day	45	592	fog	shoulder	day
17	593	normal	university	day	46	598	he. snow	highway	night
18	594	normal	urban	day	47	266	he. snow	highway	night
19	592	normal	alleyway	day	48	443	light snow	highway	night
20	595	normal	urban	day	49	598	light snow	highway	night
21	597	rain	alleyway	night	50	597	sleet	highway	night
22	598	overcast	urban	night	51	597	sleet	highway	night
23	598	rain	urban	night	52	598	sleet	highway	night
24	598	rain	urban	night	53	597	sleet	highway	day
25	597	rain	urban	night	54	601	he. snow	urban	day
26	597	rain	suburban	day	55	494	he. snow	urban	day
27	598	sleet	suburban	day	56	598	he. snow	urban	day
28	597	sleet	mountain	day	57	598	he. snow	urban	day
29	597	sleet	mountain	day	58	598	he. snow	urban	day

Table 6: Dataset composition of each sequence. ‘res.’, ‘cam.’, and ‘img.’ denotes resolution, camera, and image, respectively.

folder name	data type	extension	size	usage
radar_tesseract	4DRT	.mat	360GB	network input, visualization
radar_xyz_cube	3DRT-XYZ	.mat	72GB	network input
os1-128	High res. LPC	.pcd	14GB	network input, visualization
os2-64	Low res. LPC	.pcd	7GB	network input, visualization
cam-front	Front cam. img.	.png	4.5GB	network input, visualization
cam-left	Left cam. img.	.png	4.5GB	network input, visualization
cam-right	Right cam. img.	.png	4.5GB	network input, visualization
cam-rear	Rear cam. img.	.png	4.5GB	network input, visualization
cam-dash	Dash cam. img.	.mp4	75MB	reference video of annotation
info_calib	Calibration values	.txt	-	calibration of 4DRT and LPC
info_condition	Conditions	.txt	-	conditional evaluation
info_label	Labels	.txt	0.5MB	training, evaluation

B Details of the sensor suite

We use waterproofed sensors with grade IP66 or higher, as mentioned in Section 3.1, for safe data collection in adverse weather conditions. Table 7 summarizes the detailed information (i.e., model

name, output data format, resolution, maximum operating distance, field of view (FOV), frames per second (FPS)) of the sensors that we install for the K-Radar data collection.

Table 7: Sensor suite details: ‘Azi.’, ‘Ele.’, ‘res.’ and ‘CEP’ denotes azimuth, elevation angle, resolution, and circular error probability, respectively.

sensors	model name	output data	resolution	max range	FOV (Azi., Ele.)	FPS
4D Radar	RETINA-4ST	$64 \times 256 \times 107^\circ \times 37^\circ$ size 4D tensor	0.06m/s, 0.46m, $1^\circ, 1^\circ$	118m	$107^\circ, 37^\circ$	10
long range Lidar	os2-64	131,072 3D points	0.1cm, $0.18^\circ, 0.35^\circ$	240m	$360^\circ, 22.5^\circ$	10
high res. Lidar	os1-128	262,144 3D points	0.1cm, $0.18^\circ, 0.35^\circ$	120m	$360^\circ, 45^\circ$	10
4 stereo cameras	ZED2i	8 1280×720 size images (left, right)	1280×720 pixels	n/a	$110^\circ, 70^\circ$	30
RTK-GPS	GPS500, C94-M8P3	latitude, longitude, altitude	0.025m + 1ppm CEP	n/a	n/a	1
2 IMUs	built-in Lidar	6-axis IMU data	n/a	n/a	n/a	100

C Criteria for weather conditions, road structures, and collecting time

We establish conditions for each sequence according to the criteria in Table 8, as mentioned in Section 3.2.

Table 8: Detailed criteria for each condition.

Criteria	Name	Detailed criteria
road structures	urban	Roads with four or more lanes and traffic lights, and ego-vehicle average speed is around 60 km/h
	highway	Roads without traffic lights and ego-vehicle average speed is around 100km/h
	alleyway	Roads with two to four lanes and buildings nearby
	suburban	Two- or four-lane roads with rice paddies, fields and mountains around it
	university	The inner roads of KAIST
	mountain	Sloped roads with two to four lanes in a countryside
	parking lots	Areas for stopping or parking with other vehicles around
weather conditions	shoulder	Parking spaces by the side of the road
	normal	Clear weather that does not meet the six weather conditions below
	overcast	Sunless, cloudy weather
	fog	Weather in which distant objects are dimly visible due to omni-directional fog
	rain	Rainy weather
	sleet	Precipitation that consists of both rain and snow
	light snow	Snowfall within approximately 1 cm per hour
time zone	heavy snow	Snowfall that exceed 1 cm per hour
	day	Approximately 6:00 ~ 16:00
	night	Approximately 20:00 ~ 4:00

D Details of annotation and calibration

D.1 Details of annotation

Annotation process for calibrated LPC measurements As mentioned in Section 3.3, it is difficult to intuitively recognize the shape of objects in BEV-2D. Therefore, we utilize the calibrated LPC (Section D.2) with a maximum calibration error of 0.5cm to enable accurate 3D bounding box annotations. We include the annotation program and code in the published devkits. The annotation program supports a resolution of 1.4 cm per pixel, resulting in a maximum annotation error of 0.7 cm. The annotation program can be used by following the two steps: (1) annotate the BEV bounding box of an object in the visualized BEV LPC, (2) annotate the height and center point of the BEV bounding box. In Figure 11, we show the GUI and usage of the annotation program, and detailed instructions can be found in the video clip that is available at Section J URL 3.

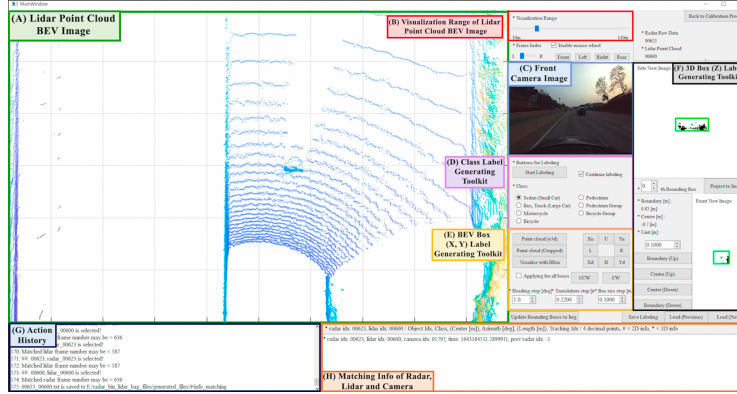


Figure 11: A snippet of the video clip that shows annotation process. (see Section J URL 3)

Annotation process in the absence of LPC measurements of objects As mentioned in Section 3.3, the annotation program we provide has a function to overlap the calibrated BEV-2D to the LPC so that annotations can be created even in the absence of LPC measurements of objects for various reasons such as adverse weather conditions. To annotate objects in the absence of LPC measurements, the human annotator processes 3D bounding box annotation by referring to overlapped BEV-2D and dash camera images of the ego-vehicle. The human annotator then verifies the height and size information of the 3D bounding box with BFS-2D, as shown in Figure 6-(b). We note that the height of the vehicle is set to a pre-defined value after checking the type of the vehicle through the dash cam image. Figure 12 illustrates the GUI of the annotation program in the absence of LPC measurements, and more detailed instructions can be found in the video clip available at Section J URL 4.

D.2 Details of the calibration between 4D Radar and Lidar

Accurate calibration of the 4DRT and LPC is crucial to utilize the 3D bounding box annotated in the LPC as a label of the 4DRT. We utilize visualized BEV-2D and LPC as well as spatial information (sensor placement location) of all sensors to precisely calibrate 4DRT and LPC. We develop a program that matches temporal offset (i.e., frame error) and spatial offset (i.e., 2D translation, yaw) through near-field (within about 30m) objects which are clearly visualized (calibration clue shown in Figure 13), as shown in Figure 14. The GUI program in Figure 14 supports a resolution of 1 cm per pixel, resulting in a maximum calibration error of 0.5 cm. We have not considered the pitch angle difference between 4D Radar and Lidar, since we fix the sensors precisely perpendicular to the ground, resulting in no theoretical difference in the pitch angle. We note that the video clip containing the calibration process (shown in Figure 14) is available in Section J URL 3, and the video clip containing the calibration result (shown in Figure 15) is available in Section J URL 5. Through the calibration process, we note that the vehicle approaching from the other side matches correctly as shown in the calibration result (shown in Figure 15).

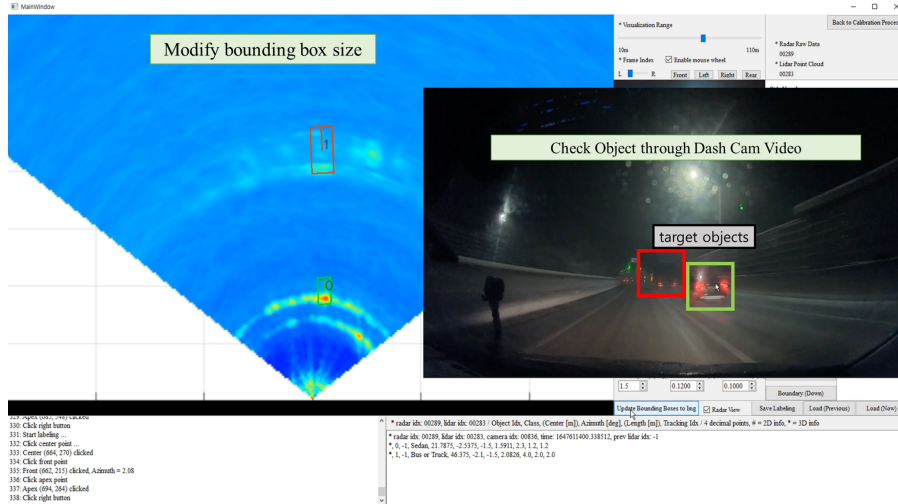


Figure 12: A snippet of the video clip that shows the annotation process in the absence of LPC measurements of objects. (see Section J URL 4)

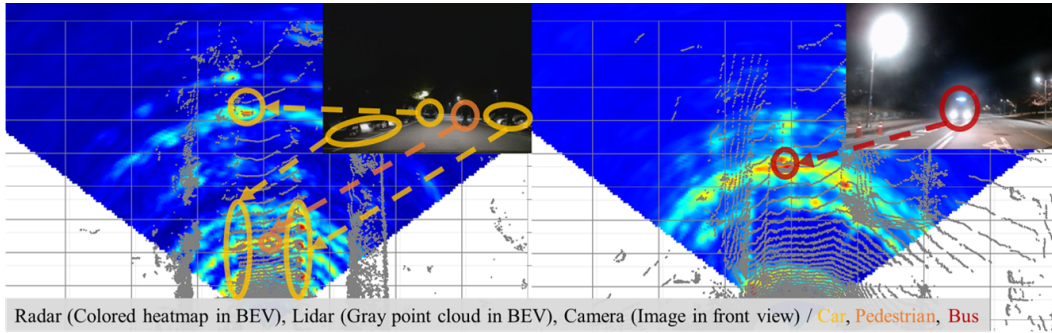


Figure 13: Examples of calibration clues.

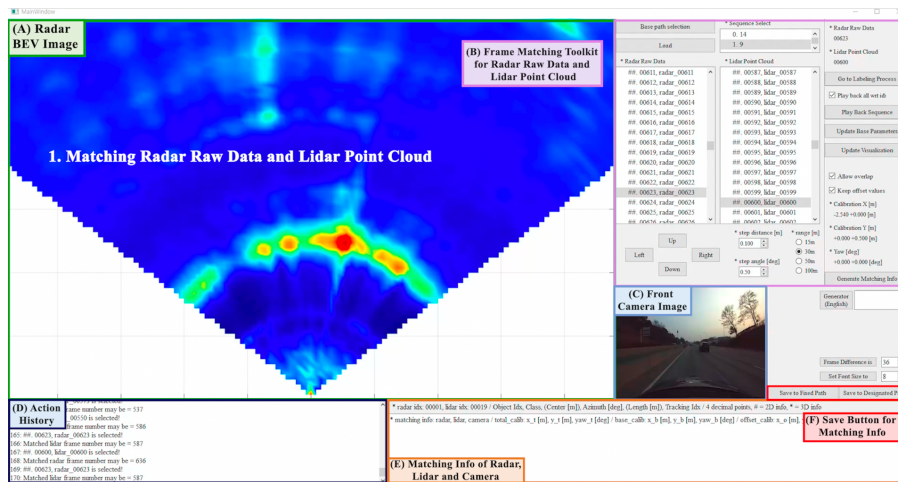


Figure 14: A snippet of the video clip that shows 4DRT/LPC calibration process through BEV-2D and LPC visualization. (see Section J URL 3)

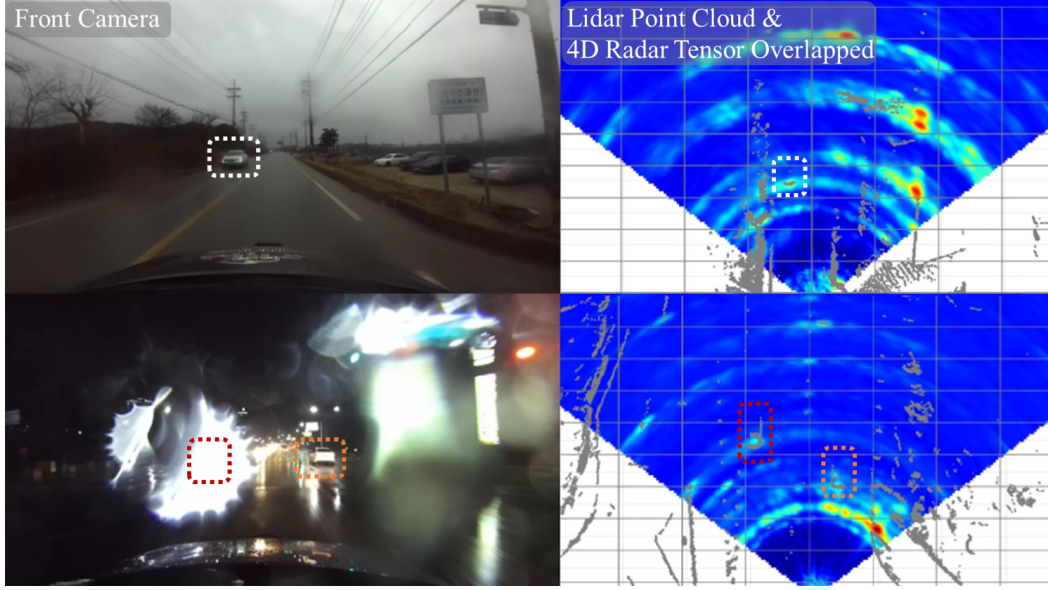


Figure 15: A snippet of the video clip that shows calibration results images for two different roads. (see Section J URL 5)

D.3 Details of the calibration between Lidar and camera

The calibration of the Lidar and camera is to determine a total of three parameters: 1) extrinsic parameters to define the relative position of the Lidar coordinate system (i.e., reference frame) and the camera coordinate system, 2) lens distortion parameters to correct camera distortion, and 3) intrinsic parameters to match each pixel in the pixel coordinate system with the points in the camera coordinate system. As shown in Figure 16, we scan a 3D model of the ego-vehicle with the sensor suite using a Lidar scanner provided in iPhone 12 Pro (Luetzenburg et al., 2021). We extract the coarse position of each sensor from the scanned 3D vehicle model. Second, we extract the lens distortion parameters and the intrinsic parameters of the camera using the camera calibration process provided by ROS (Stanford Artificial Intelligence Laboratory et al.). The previous two processes extract approximate calibration parameters, which may include calibration errors. Therefore, we construct a GUI program that can modify each parameter finely, as shown in Figure 17, and fine-tune the parameters so that the measurements of the camera and the LIDAR at the close and far objects match accurately, as shown in Figure 18.



Figure 16: The scanned 3D model of the ego-vehicle with sensor suite.

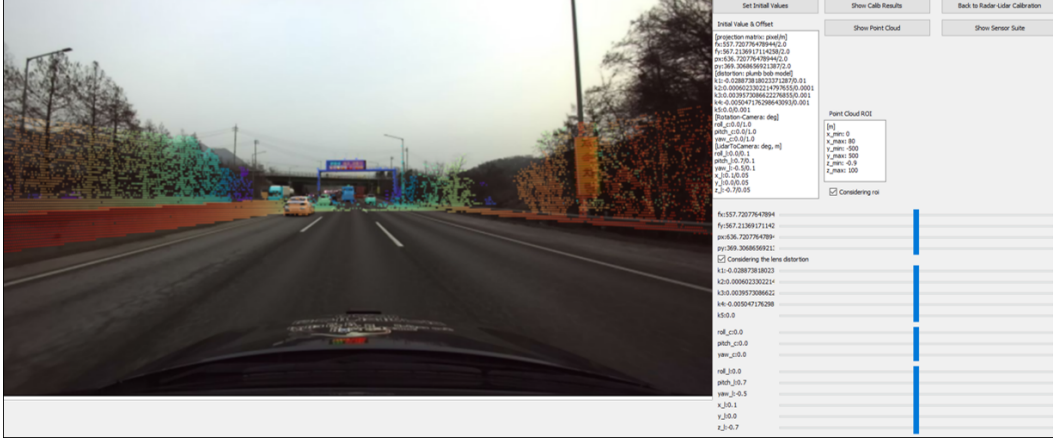


Figure 17: The GUI program to fine-tune the calibration parameters between Lidar and camera.



Figure 18: Examples of calibration result between the camera and Lidar, where colored points on the front images show the projected points of the corresponding LPCs.

In addition, we obtain the ground-truth depth value of the corresponding pixel through the points projected onto the camera image. Because the LPC is sparse, as shown in Figure 19-(b), the dense depth map is provided through interpolation, as shown in Figure 19-(c). We note that these depth maps can magnify the utilization of our dataset for the depth estimation tasks (Mertan et al., 2022), which is one of the most widely studied fields in computer vision.

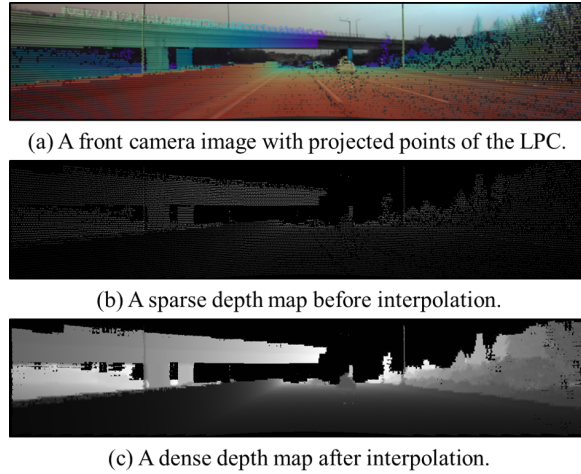


Figure 19: An example of generating a depth map based on calibration result.

E Details of baseline NNs

In this section, we describe the common structures of RTNH and RTN, neck, and head of the baseline NNs, and the structures of 3D-SCB and 2D-DCB, which are the backbone of RTNH and RTN, respectively.

E.1 Neck and head

As mentioned in Section 3.4, both RTNH and RTN extract multiple feature maps (FMs) of different resolutions. Neck transforms the FMs into the same size by applying TransposeConv2D and concatenates the transformed FMs (Lin et al., 2017a). The size of the concatenated FM is $C_{FM} \times Y_{FM} \times X_{FM}$. C_{FM} , Y_{FM} , and X_{FM} represent the number of channels of the concatenated FM, the number of grids for the left and right widths, and the number of grids for the front distance, respectively. The head predicts the bounding boxes from the concatenated FM using an anchor-based method as in Ren et al. (2015), and its structure is shown in Figure 20.

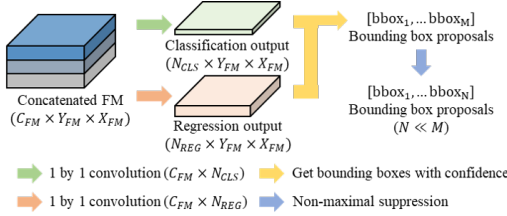


Figure 20: Head structure.

We apply 1 by 1 convolution to the concatenated FM to extract classification and regression output for each grid, as shown in Figure 20. We use two anchor boxes with yaw angles of 0° and 90° for each class, resulting in $N_{CLS} = 2(\text{Anchor}) + 1(\text{Background}) = 3$. In addition, we assign a total of eight parameters for each anchor: center point (x_c, y_c, z_c) , length, width, height (x_l, y_l, z_l) , $\cos(\text{yaw})$, and $\sin(\text{yaw})$ (Simony et al., 2018) of the bounding box, resulting in $N_{REG} = 8(N_{CLS} - 1) = 16$.

We then extract M bounding box proposals from the classification and regression outputs. In training process, proposals with an intersection over union (IOU) of 0.5 or more with respect to the ground-truth are classified as positive bounding boxes, and proposals with an IoU of less than 0.2 are classified as negative bounding boxes. We apply the focal loss (Lin et al., 2017b) to cope with the problem of class imbalance between positive bounding boxes and negative bounding boxes, and apply the smooth L1 loss between the regression value and the target value. During inference, an index with the largest logit value from the classification output is inferred as the proposal's class, and a confidence threshold of 0.3 is applied, so that low-confidence predictions are regarded as backgrounds. Thereafter, non-maximal suppression is applied to remove overlapping bounding boxes and finally a total of N bounding boxes are obtained.

E.2 3D-SCB

As mentioned in Section 3.4, we extract FMs using 3D sparse conv blocks to reduce the usage of GPU memory, while still using height information from the 4DRT. A 3D sparse conv block consists of a total of three consecutive 3D convolution layers. We set the first 3D convolution layer as 3D sparse convolution layer (Liu et al., 2015) and the remaining 3D convolution layer as 3D submanifold convolution layer (Graham et al., 2018). The output of the 3D sparse conv block is a sparse FM with four dimensions (channel, height, width, length) of different resolutions. Each sparse FM is transformed into its dense tensor counterpart, and then TransposeConv2D is applied to the three-dimensional dense FMs, resulting in dense FMs represented in BEVs with height information encoded. Finally, all dense FMs are concatenated to produce the final concatenated FM, which is the input of the head.

E.3 2D-DCB

We construct a 2D dense conv backbone (2D-DCB) with 2D conv blocks, as mentioned in Section 3.4, to extract FMs without encoding the height information. We utilize ResNet50 (He et al., 2016) and ResNext101 (Xie et al., 2017) as the 2D conv blocks whose performance has been validated on tasks such as classification (Mahajan et al., 2018) and object detection (Qiao et al., 2021). We compare object detection performance for two variations, as shown in Table 9, and in Section 4.2,

we show the results of 2D-DCB-ResNext101, which has higher performance among the two, as the representative result of RTN.

Table 9: Performance of two variants of RTN.

backbone	AP_{3D} [%]	AP_{BEV} [%]	GPU RAM [MB]
2D-DCB-ResNext101	40.12	50.67	520
2D-DCB-ResNet50	39.86	49.37	257

F Qualitative results of RTNH and PointPillars with additional discussion in various conditions

We show the object detection results of RTNH and PointPillars (Lang et al., 2019) under various weather conditions in Figure 21 and 22 with 3D bounding box labels, BEV-2D, front camera image, and LPC. We also show images from the dash camera, since some of the outdoor camera measurements are unreliable due to the adverse weather conditions.

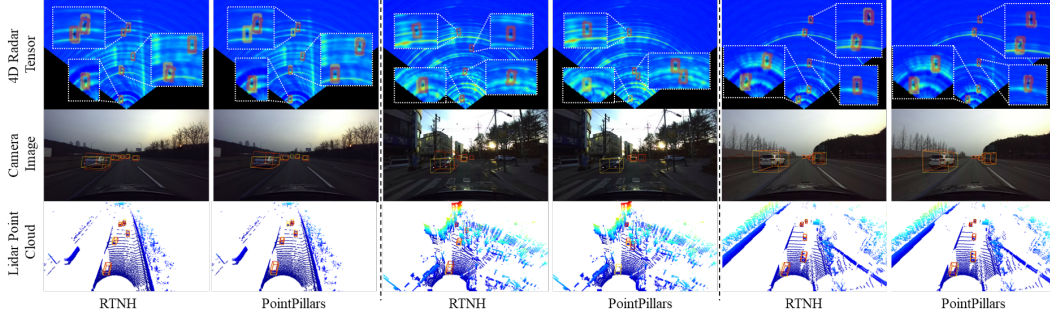


Figure 21: 3D object detection results of RTNH (4DRT) and PointPillars (LPC) in a road environment where multiple vehicles exist. We use yellow and red boxes to represent the ground truths and predictions, respectively.

Figure 21 shows the object detection results of RTNH and PointPillars for the road environments where multiple vehicles exist under weather conditions without precipitation (e.g., normal, overcast). As shown in Figure 21, RTNH produces similar or more robust detection results (robust to miss detection) compared to PointPillars. The comparisons summarized in Table 4 and Figure 21 show that 4D Radar has similar or more robust detection performance to Lidar in various road environments where multiple vehicles exist. This indicates that 4D Radar can be sufficiently used alone as a perception sensor in autonomous driving.

In addition, notice that the general AP for the normal condition can be lower than the overcast condition on K-Radar because of the following two reasons. One reason is that 4D Radar and Lidar are not affected by lighting condition, so that the detection performance of 4D Radar and Lidar for overcast condition cannot be lower than that for normal condition. Another reason is that the normal condition in K-Radar has more difficult situation than the overcast condition; the normal condition contains various situations including many vehicles parked along the side of alleyways, while the overcast condition in K-Radar does not have many vehicles on clear urban roads of two lanes, as shown in Table 5.

Figure 22 shows the object detection results of RTNH and PointPillars under weather conditions with precipitation (e.g., sleet, light snow, heavy snow). As mentioned in Section A.1, Lidar can produce reliable LPC measurements in rain and light snow condition, but not in sleet and heavy snow conditions, since the sensor surfaces are covered by frost or snow. This can be seen in the LPC in Figure 22, and also by comparing the PointPillars results in Table 4.

From the results of Figure 22 and Table 4, we demonstrate that 4D Radar is a more robust sensor than Lidar in the adverse weathers. We note that the inputs of RTNH and PointPillars are 4DRT and LPC, respectively. As mentioned in 4.3, we do not claim that RTNH is a better neural network

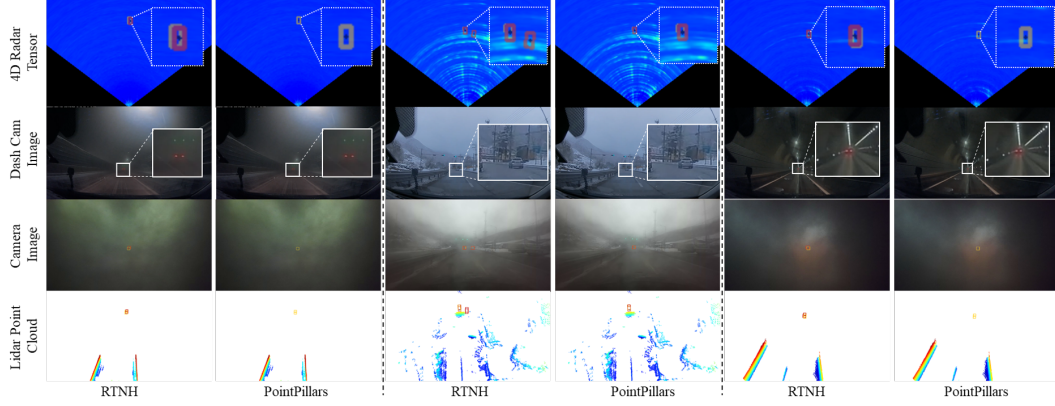


Figure 22: 3D object detection results of RTNH (4DRT) and Point Pillars (LPC) under weather conditions with precipitation. From the left, sleet, light snow, and heavy snow. We use yellow and red boxes to represent the ground truths and predictions, respectively.

architecture compared to PointPillars. Instead, we demonstrate the robustness of 4D Radar in all weather conditions including adverse weathers.

G Consideration of the K-Radar dataset as a pre-training dataset for other Radar tensor datasets

Pre-training on large scale datasets is well known to help neural networks converge faster (He et al., 2019). Therefore, we may consider using K-Radar as a pre-training dataset for other Radar tensor-based object detection datasets, or conversely, using other datasets as a pre-training dataset for K-Radar.

However, we want to note that the pre-training on K-Radar does not directly guarantee a strong improvement on RADIATE. This is because the characteristics of K-Radar and RADIATE are inherently different.

First, the power measurements in K-Radar and RADIATE have different distributions due to the different type of Radars used. When a neural network is trained on a dataset and applied to process target data of different distribution, there will be a poorly degraded performance in the target domain, as we see in Lidar object detection networks trained and evaluated on different type of point clouds (e.g., Velodyne and Ouster) (Wang et al., 2020).

Second, the resolution of RADIATE (0.175m) is higher than K-Radar (0.46m). This mismatch of resolution can also adversely affect the detection performance as usually seen in Lidar object detection networks trained on NuScenes (32-channels) and evaluated on KITTI (64-channels) (Wang et al., 2020).

Third, the data distributions are significantly different. K-Radar data is collected in South Korea where cars drive on the right, while RADIATE is collected in the U.K where cars drive on the left.

The above reasons apply to other Radar tensor-based datasets as well as RADIATE. For these reasons, it is difficult to expect performance improvement by using K-Radar as a pre-training dataset for other Radar tensor-based datasets and vice versa.

H Performance of RTNH on wider areas and multiple classes

We present the detection performance of RTNH over broader areas and multiple classes in Table 10. The results in Table 10 differ from those in Table 4 in two main aspects: Firstly, the evaluation extends from a narrow to a wider scope with dimensions of x, y, z in the ranges of 0 to 72, -16 to 16, and -2 to 7.6 meters, respectively. Secondly, the performance now encompasses the Bus or Truck class alongside the Sedan class, thereby representing both compact and large vehicle categories.

Moreover, we indicate the performance of the Bus or Truck class with a '-' for both rain and sleet conditions, as they are not present under these conditions.

Table 10: Performance of RTNH on wider areas and multiple classes

Class	Metric	Total	normal	over-cast	fog	rain	sleet	light snow	heavy snow
Sedan	$AP_{3D} [\%]$	48.2	45.5	58.8	79.3	40.3	48.1	65.6	52.6
	$AP_{BEV} [\%]$	56.7	53.8	68.3	89.6	49.3	55.6	69.4	60.3
Bus or Truck	$AP_{3D} [\%]$	34.4	25.3	31.1	-	-	28.5	78.2	46.3
	$AP_{BEV} [\%]$	45.3	31.8	32.0	-	-	34.4	89.3	78.0

I Details of devkits

To facilitate the experiments on various neural network structures, we provide modularized neural network training codes that can manage each experiment with a single configuration file. We also provide GUI-based programs for visualization and neural network inference, as shown in Figure 23, to facilitate inference on large amounts of data. We provide a video clip on how to use the program, which can be found through Section J URL 6, and all codes for devkits can be downloaded from Section J URL 1.

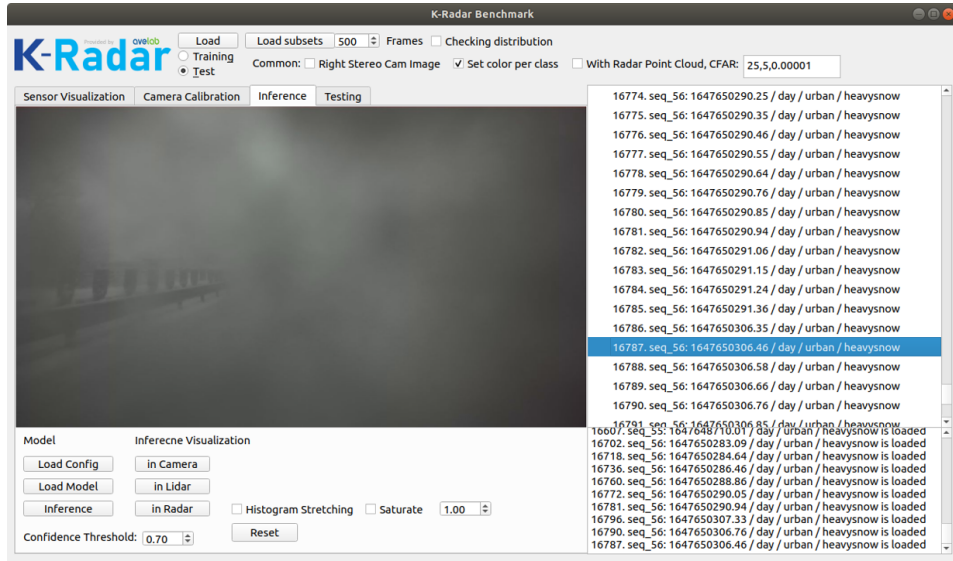


Figure 23: A snippet of the video clip that shows GUI-based program for visualization and neural network inference. (see Section J URL 6)

J Relevant URLs

- (1) Publication of datasets and complete devkits code (learning, evaluation, reasoning, visualization, labeling programs): <https://github.com/kaist-avelab/K-Radar>
- (2) The video clip showing each sensor measurement dynamically changing during driving under the heavy snow condition: <https://www.youtube.com/watch?v=TZh5i2eLp1k&t=103s>
- (3) The video clip showing the 4DRT/LPC calibration and annotation process: <https://www.youtube.com/watch?v=y1G0USHCBpU&t=152s>
- (4) The video clip showing the annotation process in the absence of LPC measurements of objects: https://www.youtube.com/watch?v=IL1BJJpm4_4&t=8s

- (5) The video clip showing calibration results: <https://www.youtube.com/watch?v=U4qkaMSJ0ds&t=10s>
- (6) The video clip showing the GUI-based program for visualization and neural network inference: <https://www.youtube.com/watch?v=MrFPv01ZjTY&t=3s>
- (7) The video clip showing the information regarding tracking for multiple objects on the roads: https://www.youtube.com/watch?v=8mqxf58_ZAk

References

- Dong-Hee Paek, Seung-Hyun Kong, and Kevin Tirta Wijaya. K-lane: Lidar lane dataset and benchmark for urban roads and highways. In *Proceedings of the IEEE/CVF Conference on Computer Vision and Pattern Recognition (CVPR) Workshops*, June 2022.
- Lizhe Liu, Xiaohao Chen, Siyu Zhu, and Ping Tan. Condlanenet: a top-to-down lane detection framework based on conditional convolution. In *Proceedings of the IEEE/CVF International Conference on Computer Vision*, pages 3773–3782, 2021.
- Chien-Yao Wang, Alexey Bochkovskiy, and Hong-Yuan Mark Liao. Scaled-yolov4: Scaling cross stage partial network. In *Proceedings of the IEEE/cvf conference on computer vision and pattern recognition*, pages 13029–13038, 2021a.
- Alex H Lang, Sourabh Vora, Holger Caesar, Lubing Zhou, Jiong Yang, and Oscar Beijbom. Pointpillars: Fast encoders for object detection from point clouds. In *Proceedings of the IEEE/CVF Conference on Computer Vision and Pattern Recognition*, pages 12697–12705, 2019.
- Bence Major, Daniel Fontijne, Amin Ansari, Ravi Teja Sukhavasi, Radhika Gowaikar, Michael Hamilton, Sean Lee, Slawomir Grzechnik, and Sundar Subramanian. Vehicle detection with automotive radar using deep learning on range-azimuth-doppler tensors. In *2019 IEEE/CVF International Conference on Computer Vision Workshop (ICCVW)*, pages 924–932, 2019. doi: 10.1109/ICCVW.2019.00121.
- René Ranftl, Alexey Bochkovskiy, and Vladlen Koltun. Vision transformers for dense prediction. In *Proceedings of the IEEE/CVF International Conference on Computer Vision*, pages 12179–12188, 2021.
- Zachary Teed and Jia Deng. Droid-slam: Deep visual slam for monocular, stereo, and rgb-d cameras. *Advances in Neural Information Processing Systems*, 34, 2021.
- Akhil Kurup and Jeremy Bos. Dsor: A scalable statistical filter for removing falling snow from lidar point clouds in severe winter weather. *arXiv preprint arXiv:2109.07078*, 2021.
- Fahad Jibrin Abdu, Yixiong Zhang, Maozhong Fu, Yuhua Li, and Zhenmiao Deng. Application of deep learning on millimeter-wave radar signals: A review. *Sensors*, 21(6), 2021. ISSN 1424-8220. doi: 10.3390/s21061951.
- Xu Dong, Pengluo Wang, Pengyue Zhang, and Langechuan Liu. Probabilistic oriented object detection in automotive radar. In *Proceedings of the IEEE/CVF Conference on Computer Vision and Pattern Recognition (CVPR) Workshops*, June 2020.
- Mohammadreza Mostajabi, Ching Ming Wang, Darsh Ranjan, and Gilbert Hsyu. High resolution radar dataset for semi-supervised learning of dynamic objects. In *2020 IEEE/CVF Conference on Computer Vision and Pattern Recognition Workshops (CVPRW)*, pages 450–457, 2020. doi: 10.1109/CVPRW50498.2020.00058.
- Marcel Sheeny, Emanuele De Pellegrin, Saptarshi Mukherjee, Alireza Ahrabian, Sen Wang, and Andrew Wallace. Radiate: A radar dataset for automotive perception in bad weather. In *2021 IEEE International Conference on Robotics and Automation (ICRA)*, pages 1–7. IEEE, 2021.
- Andreas Geiger, Philip Lenz, and Raquel Urtasun. Are we ready for autonomous driving? the kitti vision benchmark suite. In *2012 IEEE Conference on Computer Vision and Pattern Recognition*, pages 3354–3361, 2012. doi: 10.1109/CVPR.2012.6248074.
- Pei Sun, Henrik Kretschmar, Xerxes Dotiwalla, Aurelien Chouard, Vijaysai Patnaik, Paul Tsui, James Guo, Yin Zhou, Yuning Chai, Benjamin Caine, et al. Scalability in perception for autonomous driving: Waymo open dataset. In *Proceedings of the IEEE/CVF conference on computer vision and pattern recognition*, pages 2446–2454, 2020.
- Holger Caesar, Varun Bankiti, Alex H. Lang, Sourabh Vora, Venice Erin Liong, Qiang Xu, Anush Krishnan, Yu Pan, Giancarlo Baldan, and Oscar Beijbom. nuscenes: A multimodal dataset for autonomous driving. In *Proceedings of the IEEE/CVF Conference on Computer Vision and Pattern Recognition (CVPR)*, June 2020.

- Ramin Nabati and Hairong Qi. Centerfusion: Center-based radar and camera fusion for 3d object detection. In *Proceedings of the IEEE/CVF Winter Conference on Applications of Computer Vision*, pages 1527–1536, 2021.
- Arthur Ouaknine, Alasdair Newson, Julien Rebut, Florence Tupin, and Patrick Perez. Carrada dataset: Camera and automotive radar with range-angle-doppler annotations. In *2020 25th International Conference on Pattern Recognition (ICPR)*, pages 5068–5075. IEEE, 2021.
- Ao Zhang, Farzan Erlik Nowruzi, and Robert Laganieri. Raddet: Range-azimuth-doppler based radar object detection for dynamic road users. In *2021 18th Conference on Robots and Vision (CRV)*, pages 95–102. IEEE, 2021.
- Yizhou Wang, Gaoang Wang, Hung-Min Hsu, Hui Liu, and Jenq-Neng Hwang. Rethinking of radar’s role: A camera-radar dataset and systematic annotator via coordinate alignment. In *Proceedings of the IEEE/CVF Conference on Computer Vision and Pattern Recognition (CVPR) Workshops*, pages 2815–2824, June 2021b.
- Andras Palffy, Ewoud Pool, Srimannarayana Baratam, Julian F. P. Kooij, and Darius M. Gavrilă. Multi-class road user detection with 3+1d radar in the view-of-delft dataset. *IEEE Robotics and Automation Letters*, 7(2): 4961–4968, 2022. doi: 10.1109/LRA.2022.3147324.
- Michael Meyer and Georg Kusch. Automotive radar dataset for deep learning based 3d object detection. In *2019 16th European Radar Conference (EuRAD)*, pages 129–132, 2019.
- Fisher Yu, Haofeng Chen, Xin Wang, Wenqi Xian, Yingying Chen, Fangchen Liu, Vashisht Madhavan, and Trevor Darrell. Bdd100k: A diverse driving dataset for heterogeneous multitask learning. In *Proceedings of the IEEE/CVF conference on computer vision and pattern recognition*, pages 2636–2645, 2020.
- Stefan Briskén, Florian Ruf, and Felix Höhne. The recent evolution of automotive imaging radar and its information content. *IET Radar, Sonar, Navigation*, 12, 04 2018. doi: 10.1049/iet-rsn.2018.0026.
- Baoyuan Liu, Min Wang, Hassan Foroosh, Marshall Tappen, and Marianna Pensky. Sparse convolutional neural networks. In *2015 IEEE Conference on Computer Vision and Pattern Recognition (CVPR)*, pages 806–814, 2015. doi: 10.1109/CVPR.2015.7298681.
- Yue Zhou, Shengjie Niu, Jingjing Lü, and Yuehua Zhou. The effect of freezing drizzle, sleet and snow on microphysical characteristics of supercooled fog during the icing process in a mountainous area. *Atmosphere*, 7:143, 11 2016. doi: 10.3390/atmos7110143.
- Gregor Luetzenburg, Aart Kroon, and Anders Bjørk. Evaluation of the apple iphone 12 pro lidar for an application in geosciences. *Scientific Reports*, 11, 11 2021.
- Stanford Artificial Intelligence Laboratory et al. Robotic operating system. URL <https://www.ros.org>.
- Alican Mertan, Damien Jade Duff, and Gozde Unal. Single image depth estimation: An overview. *Digital Signal Processing*, page 103441, 2022.
- Tsung-Yi Lin, Piotr Dollár, Ross Girshick, Kaiming He, Bharath Hariharan, and Serge Belongie. Feature pyramid networks for object detection. In *Proceedings of the IEEE conference on computer vision and pattern recognition*, pages 2117–2125, 2017a.
- Shaoqing Ren, Kaiming He, Ross Girshick, and Jian Sun. Faster r-cnn: Towards real-time object detection with region proposal networks. *Advances in neural information processing systems*, 28, 2015.
- Martin Simony, Stefan Milzy, Karl Amendey, and Horst-Michael Gross. Complex-yolo: An euler-region-proposal for real-time 3d object detection on point clouds. In *Proceedings of the European Conference on Computer Vision (ECCV) Workshops*, pages 0–0, 2018.
- Tsung-Yi Lin, Priya Goyal, Ross Girshick, Kaiming He, and Piotr Dollár. Focal loss for dense object detection. In *Proceedings of the IEEE international conference on computer vision*, pages 2980–2988, 2017b.
- Benjamin Graham, Martin Engelcke, and Laurens Van Der Maaten. 3d semantic segmentation with submanifold sparse convolutional networks. In *Proceedings of the IEEE conference on computer vision and pattern recognition*, pages 9224–9232, 2018.
- Kaiming He, Xiangyu Zhang, Shaoqing Ren, and Jian Sun. Deep residual learning for image recognition. In *Proceedings of the IEEE conference on computer vision and pattern recognition*, pages 770–778, 2016.
- Saining Xie, Ross Girshick, Piotr Dollár, Zhuowen Tu, and Kaiming He. Aggregated residual transformations for deep neural networks. In *Proceedings of the IEEE conference on computer vision and pattern recognition*, pages 1492–1500, 2017.

- Dhruv Mahajan, Ross Girshick, Vignesh Ramanathan, Kaiming He, Manohar Paluri, Yixuan Li, Ashwin Bharambe, and Laurens Van Der Maaten. Exploring the limits of weakly supervised pretraining. In *Proceedings of the European conference on computer vision (ECCV)*, pages 181–196, 2018.
- Siyuan Qiao, Liang-Chieh Chen, and Alan Yuille. Detectors: Detecting objects with recursive feature pyramid and switchable atrous convolution. In *Proceedings of the IEEE/CVF conference on computer vision and pattern recognition*, pages 10213–10224, 2021.
- Kaiming He, Ross Girshick, and Piotr Dollár. Rethinking imagenet pre-training. In *Proceedings of the IEEE/CVF International Conference on Computer Vision*, pages 4918–4927, 2019.
- Yan Wang, Xiangyu Chen, Yurong You, Li Erran Li, Bharath Hariharan, Mark Campbell, Kilian Q Weinberger, and Wei-Lun Chao. Train in germany, test in the usa: Making 3d object detectors generalize. In *Proceedings of the IEEE/CVF Conference on Computer Vision and Pattern Recognition*, pages 11713–11723, 2020.